Nanoscale Advances

ROYAL SOCIETY OF CHEMISTRY

PAPER

View Article Online
View Journal

Cite this: DOI: 10.1039/d6na00352d

Strain-driven electronic phase transition and quantum transport signatures in epitaxial bismuth films on silicon substrates

Jicheng Zhao, Yuxiang Dai, Chang Gao* and Yang Qi*

Bismuth (Bi), a canonical semimetal with giant spin–orbit coupling, is a prime candidate for hosting exotic topological phases of matter. Strain engineering offers a powerful pathway to manipulate its electronic ground state, yet systematic experimental validation remains elusive. Here, we demonstrate a strain-driven electronic phase transition in epitaxial Bi films grown on Si substrates *via* molecular beam epitaxy (MBE). A combination of *in situ* electron diffraction and *ex situ* X-ray diffraction reveals that coherent compressive strain, induced by lattice mismatch, systematically relaxes as the film thickness surpasses a critical value of approximately 150 Å. In the highly strained regime, the films exhibit a quasi-insulating behavior, consistent with the theoretically predicted strain-induced opening of a bulk band gap–a key prerequisite for a topological phase transition. As the strain relaxes, the system reverts to its intrinsic semimetallic state. This transition is directly mirrored in the electronic transport properties, where the evolution of a low-temperature resistivity anomaly provides a clear signature of weak localization, reflecting changes in electronic coherence and disorder. Our work establishes a direct correlation between epitaxial strain, electronic structure, and quantum transport phenomena in Bi, providing a comprehensive experimental framework for exploring strain-engineered topological states in quantum materials.

Received 1st May 2026
Accepted 8th May 2026

DOI: 10.1039/d6na00352d

rsc.li/nanoscale-advances

Introduction

Bismuth (Bi), a semimetal with a unique topological electronic structure, is regarded as a highly promising silicon-compatible thermoelectric material due to its high carrier mobility and excellent Seebeck coefficient.[1–6] However, due to the significant lattice mismatch between Bi and Si, epitaxial growth of Bi films on Si substrates introduces in-plane stress.[7–10] This profoundly alters their intrinsic electronic properties, presenting both challenges and opportunities for device applications.[11–13]

To fabricate high-quality Bi polycrystalline films, continuous optimization of the fabrication process is essential.[14–16] Among the critical factors influencing Bi film growth are substrate temperature and film thickness. Lattice mismatch, as a core physical parameter in heteroepitaxial growth, is one of the decisive factors regulating the microstructure and macroscopic properties of bismuth films.[16–22] As a semimetal, Bi exhibits a unique band structure that is highly sensitive to changes in lattice constants.[23–27] Lattice mismatch with the substrate induces compressive or tensile stress, significantly altering the relative positions of its valence band maximum (VBM) and conduction band minimum (CBM).[28–33] This stress-induced band modulation can cause the electronic properties of Bi films to transition between semimetallic, semiconductor, and even topological insulator states.[34–38] The magnitude of lattice mismatch directly influences the critical thickness of the film, which determines its crystalline quality, surface morphology, and grain orientation.[39–42] Therefore, a deep understanding and precise control of lattice mismatch are crucial for achieving high-performance applications of bismuth films.

D. Meyer *et al.*[43] demonstrated a technique using spot profile analysis low-energy electron diffraction (SPA-LEED) to precisely measure the strain state *in situ* during the epitaxial growth of Bi(111) films on Si(001) substrates. By utilizing two non-equivalent integer-order diffraction points originating from the two Bi sublattices, their method allows for high-precision determination of the film's lattice parameters, enabling the tracking of strain evolution during growth. Other studies have explored mismatch effects in different material systems. P. A. Gabrys *et al.*,[44] for instance, grew heteroepitaxial colloidal films using DNA-modified nanoparticles as programmable 'atomic equivalents', finding that more flexible and compliant building blocks better accommodate mismatches and the resulting strains. Their study also demonstrated that the films exhibit markedly different relaxation behaviors in positive (tensile) *versus* negative (compressive) lattice mismatch regimes. In the context of functional oxides, Li *et al.*[45] investigated the effect of mismatch stress on the domain structure and domain wall

School of Materials Science and Engineering, Northeastern University, China. E-mail: Bryce1003@outlook.com; daiyuxiang@mail.neu.edu.cn; gaochang@mail.neu.edu.cn; qiyang@imp.neu.edu.cn

(DW) conductivity of lithium niobate thin films. Their results indicated that while the mismatch strain did not change the overall domain structure, it significantly affected the polarization intensity. Moreover, they showed that the DW conductivity could be effectively enhanced through careful engineering of the mismatch stress. Despite these advances, systematic investigations of compressive stress in Bi films on Si substrates are still lacking. Most existing studies have been limited to confirming the presence of stress or measuring a static critical thickness. Consequently, a clear physical picture supported by direct experimental evidence—detailing how the dynamic process of stress relaxation as a function of thickness continuously modulates the electronic transport properties—remains elusive.

This study systematically investigates the complete evolution process of the critical thickness, rather than focusing solely on a single thickness point. By integrating reflection electron diffraction (RHEED), X-ray diffraction (XRD), X-ray photoelectron spectroscopy (XPS), resistance–temperature (R–T), and Hall measurement data, a mutually corroborating chain of evidence has been established. The study provides an in-depth elucidation of the stress relaxation mechanism and its regulatory effect on electronic properties.

Experimental

The bismuth evaporation process was conducted in an ultra-high vacuum (UHV) molecular beam epitaxy (MBE) system employing a boron nitride crucible as the thermal source container. A resistance-heated beam source furnace provided precise thermal control for the evaporation process. Prior to deposition, Si(100), Si(110), and Si(111) substrates were ultrasonically cleaned and then inverted on a molybdenum sample holder to ensure optimal thermal contact. *C*-axis-oriented Bi epitaxial films were synthesized under UHV with a base pressure below 1×10^{-7} Pa and operational pressure maintained at 5×10^{-7} Pa. The deposition rate was precisely regulated between 0.6 and 1.9 Å min^{-1} through computer-controlled shutter operation, while substrate temperatures were maintained within the 70–130 °C range using a PID-regulated heating stage. Film thickness calibration was achieved through a dual measurement protocol: real-time monitoring using a quartz crystal microbalance followed by post-deposition verification with a Dektak3 surface profilometer. Structural characterization was performed using a Rigaku-D/max-A X-ray diffractometer equipped with Cu Kα radiation, confirming the crystalline orientation and phase purity of the films. Surface morphology analysis was conducted using a Nanoscan Easy2 atomic force microscope operating in intermittent contact mode. X-ray photoelectron spectroscopy (XPS) measurements were conducted on a Shimadzu AXIS Supra+ spectrometer. The transport properties were characterized using a physical property measurement system (PPMS, Quantum Design, DynaCool-9) equipped with a high precision rotator and the magnetic field up to 9 T.

Results and discussion

Fig. 1a, c and e shows the XRD patterns of Bi films deposited on Si(100), Si(110), and Si(111) substrates at a substrate temperature of 70 °C and a deposition rate of 1 Å min^{-1}, within a thickness range of 90 Å to 240 Å. The hexagonal structure was indexed in this study, with the standard PDF card number 05-0519 and lattice constants $a = 4.546$ Å, $b = 4.546$ Å, and $c = 11.86$ Å. The 2θ diffraction peaks of the Bi film on the three substrates appear at 22.480°, 45.889°, and 71.468°, corresponding to the (003), (006), and (009) crystal planes of Bi, respectively. Comparison with the standard PDF reveals no significant peak position shifts. The intensity of the (001) crystal plane diffraction peak increases with film thickness, indicating that the Bi film exhibits a highly preferred orientation. On Si(100) and Si(110) substrates, when the film thickness reached 240 Å, the XRD pattern exhibited a (012) plane at 27.165°, though its intensity was lower than that of the (003) plane. The competitive growth of the (003) and (012) planes is crucial for bismuth films. The emergence of the (012) plane occurs because the film exceeds the critical thickness, releasing in-plane stress and shifting the growth mechanism from substrate-dominated to film-energy-dominated. After growing along the (012) plane, the film cannot undergo reconstruction, resulting in prominent unit cells on the film surface.

To investigate the effect of film thickness on crystallinity in Bi films grown on three substrates, statistical analysis was performed on the full width at half maximum (FWHM) and grain size of the (003) plane diffraction peak in the XRD patterns, as shown in Fig. 1b, d and f. The FWHM of the (003) plane decreased with increasing film thickness, indicating enhanced crystallinity. Conversely, the grain size exhibited opposite behavior, showing a marked increase as the film thickness increased from 90 Å to 240 Å. Based on the differing slopes of the curves, film growth can be divided into two stages: stage I: the film thickness between 90 Å and 150 Å. The grain size rapidly increased during this stage, with grains coarsening quickly. The improved crystalline quality of the film led to a rapid decrease in the FWHM. Stage II: spanning film thicknesses from 150 Å to 240 Å, where the growth rate of the grain size decreases. At this point, grains have already reached a considerable size, and the driving force for the system to reduce total energy through grain boundary migration is less pronounced than that in the first stage. Although grains continue to grow slowly, the rate is significantly reduced. The difference in grain size growth rates reflects the change in the film growth mechanism.

XPS characterization determined the elemental composition of the Bi film. The peak positions of the Bi 4f core levels were calibrated using the C 1s spectrum, with the standard based on the 284.8 eV binding energy of C 1s, as shown in Fig. 2a. Fig. 2b displays the spin–orbit doublet of Bi 4f in the Bi film. The XPS spectra of the Bi 4f core level exhibit binding energies of 156.9 eV at Bi $4f_{7/2}$ and 162.2 eV at Bi $4f_{5/2}$, characteristic of the Bi–Bi bond. No characteristic signals for Bi–Bi bond oxidation were observed in the XPS spectrum. To directly probe the

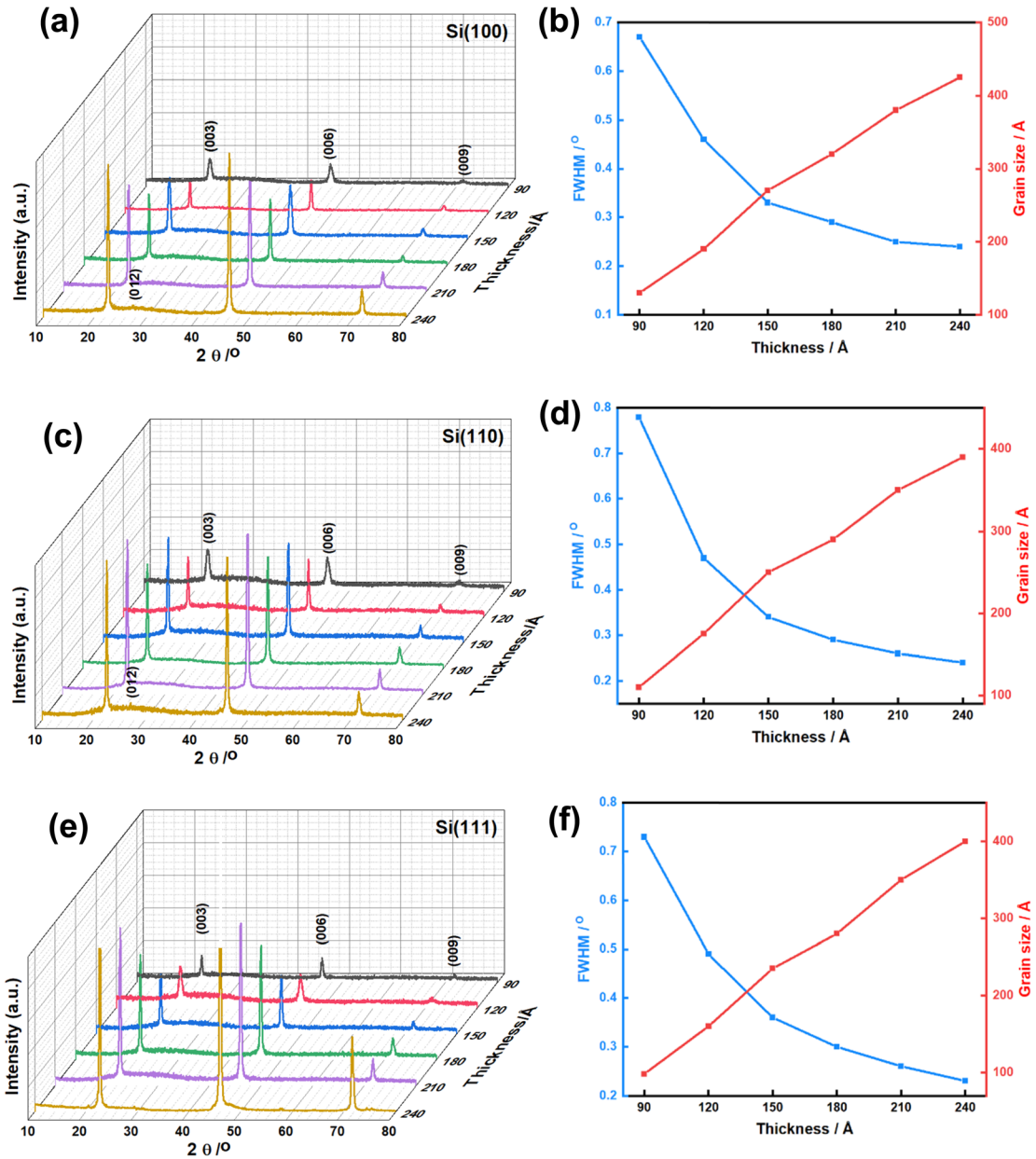

Fig. 1 (a) XRD patterns of Bi films on Si(100) substrates with varying film thicknesses. (b) FWHM and out-of-plane grain size of Bi films on Si(100) substrates. (c) XRD patterns of Bi films on Si(110) substrates with varying film thicknesses. (d) FWHM and the out-of-plane grain size of Bi films on Si(110) substrates. (e) XRD patterns of Bi films on Si(111) substrates with varying film thicknesses. (f) FWHM and the out-of-plane grain size of Bi films on Si(111) substrates.

modulation of the electronic structure in Bi films by compressive stress relaxation, XPS valence band spectra with a reference Au Fermi edge were acquired for representative thicknesses (90 Å and 210 Å), as shown in Fig. 2c. A systematic evolution of the valence band spectrum was observed as the film thickness increased from 90 Å to 210 Å. The most prominent feature is the distinct shift of the VBM. Using first-derivative analysis for precise localization, we determined the VBM positions for Bi films of 90 Å and 210 Å thickness to be 0.37 eV and 0.12 eV, respectively. The 90 Å spectrum appears to exhibit an additional shoulder-like structure around the Fermi energy. We interpret this near the Fermi energy spectral weight as arising from surface states or quantum well states that are more prominent in thinner films. This interpretation is consistent with previous angle-resolved photoemission spectroscopy (ARPES) studies on Bi films,[36] which demonstrated that for films below ~120 Å, the top and bottom surface states couple to form quantized sub bands, some of which cross and contribute to the spectral weight near the Fermi energy. The absence of this feature in the 210 Å film can be attributed to the decoupling of the two surfaces and the recovery of the bulk-like electronic structure. The VBM shift indicates a reduction in the energy barrier for

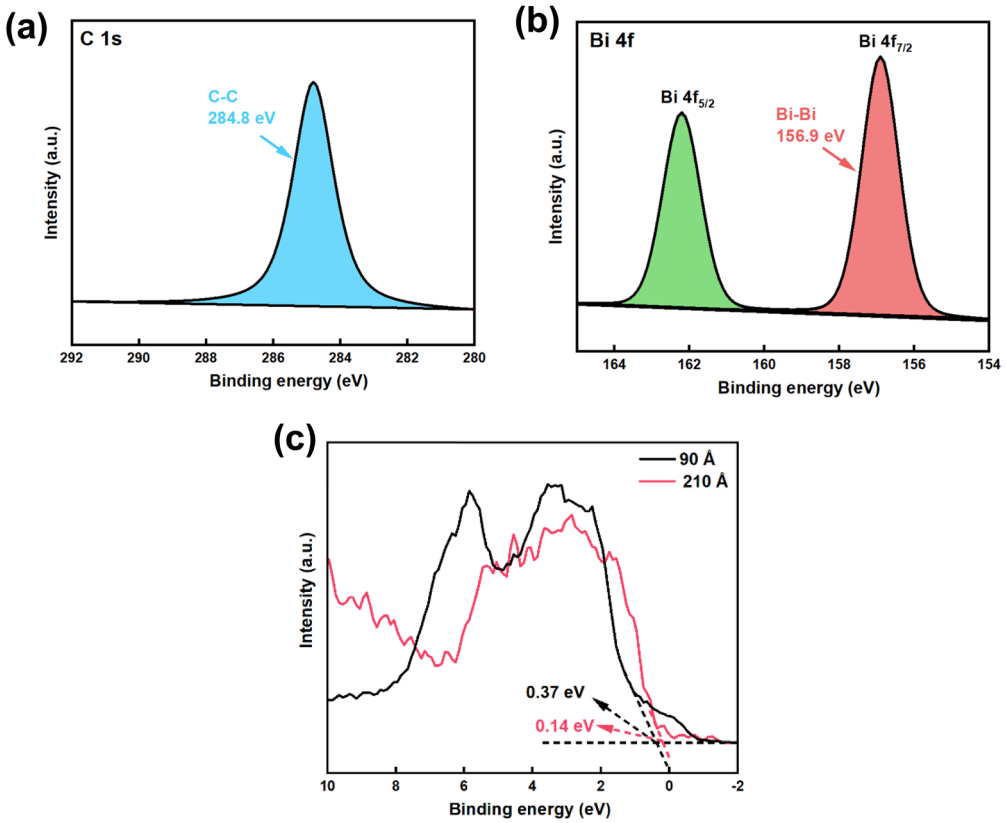

Fig. 2 (a) High resolution XPS spectrum of C 1s of Bi films. (b) High resolution XPS spectrum of Bi 4f core levels of Bi films. (c) XPS valence band spectrum of Bi films with thicknesses of 90 Å and 210 Å.

hole excitation, directly corresponding to the increased carrier concentration observed in Hall measurements. This suggests that semimetallic properties are restored after relaxation, with an increased number of carrier states available for conducting electricity. This trend is fully consistent with the enhanced metallic behavior observed in the high-temperature region of the *R–T* curve.

Fig. 3 shows the AFM surface topography of Bi films with different thicknesses on Si(100), Si(110), and Si(111) substrates, with a scanning area of 2 μm × 2 μm. At 90 Å, the AFM image reveals a surface composed of fine, dense, and interconnected two-dimensional islands. The Bi film exhibits low surface roughness with shallow channels between islands. This indicates that the film follows a layered growth pattern, where Bi atomic layers epitaxially grow under strong confinement on the Si substrate. Surface undulations primarily reflect the coalescence process of initial nucleation islands. At 150 Å, the original two-dimensional islands begin to fuse and bulge upward, revealing irregular wrinkles oriented in various directions and an increase in surface roughness. This provides direct evidence of local buckling or slip occurring within the film during stress relaxation. At 210 Å, the AFM image of the Bi film consists of distinct, isolated large-sized grains separated by pronounced deep grooves. The evolution of the AFM morphology provides direct topographical evidence for stress relaxation with thickness. This evolution is highly consistent with results from RHEED, XRD, and electrical transport measurements.

In situ reflection high-energy electron diffraction (RHEED) was utilized to monitor the epitaxial growth process and to determine the specific epitaxial relationship between the Bi films and the Si substrates. The diffraction spots are clear and bright, indicating a contamination-free substrate surface. The lattice constants of the three substrates were calculated from the diffraction fringe spacing and matched the room-temperature lattice constants of the three substrates. Fig. 4d, e and f present schematic diagrams illustrating the matching configurations between Bi films and Si(100), Si(110), and Si(111) substrates. By rotating the sample stage during Bi film growth and observing changes in the RHEED patterns, the matching modes between the three substrates and the Bi films can be determined. Based on the matching configurations of the three substrates shown in the figure, the mismatch between the Bi film and the substrates was determined. The mismatch for Si(100) is 1.36%, for Si(110) is 2.32%, and for Si(111) is 1.31%.

As shown in Fig. 5, by monitoring RHEED measurements of Bi films grown on Si(100), Si(110), and Si(111) substrates, we can clearly trace the evolution of the in-plane lattice constant gradually increasing with film thickness. This phenomenon directly reveals the kinetic mechanism of compressive stress relaxation. On the Si(100) substrate, the lattice constants of the Bi film at thicknesses of 90 Å, 120 Å, 150 Å, and 180 Å were 4.511

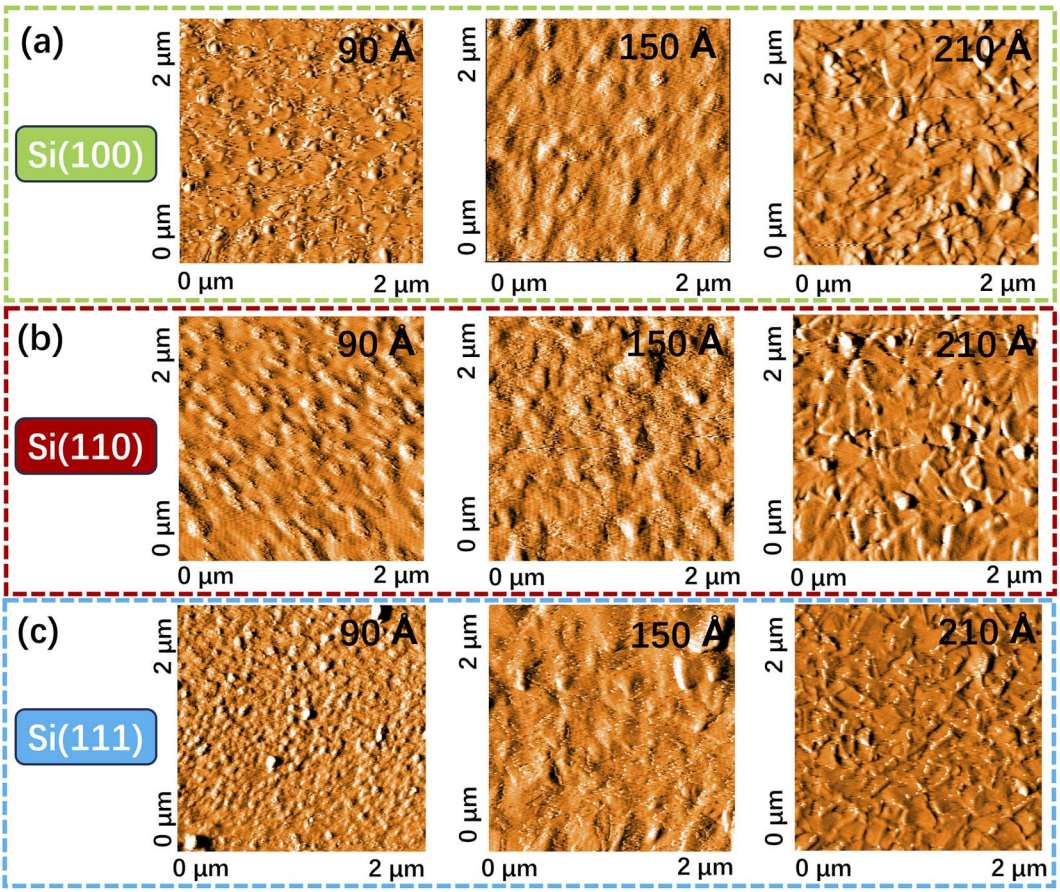

Fig. 3 AFM images of Bi films fabricated at different film thicknesses on (a) Si(100), (b) Si(110), and (c) Si(111).

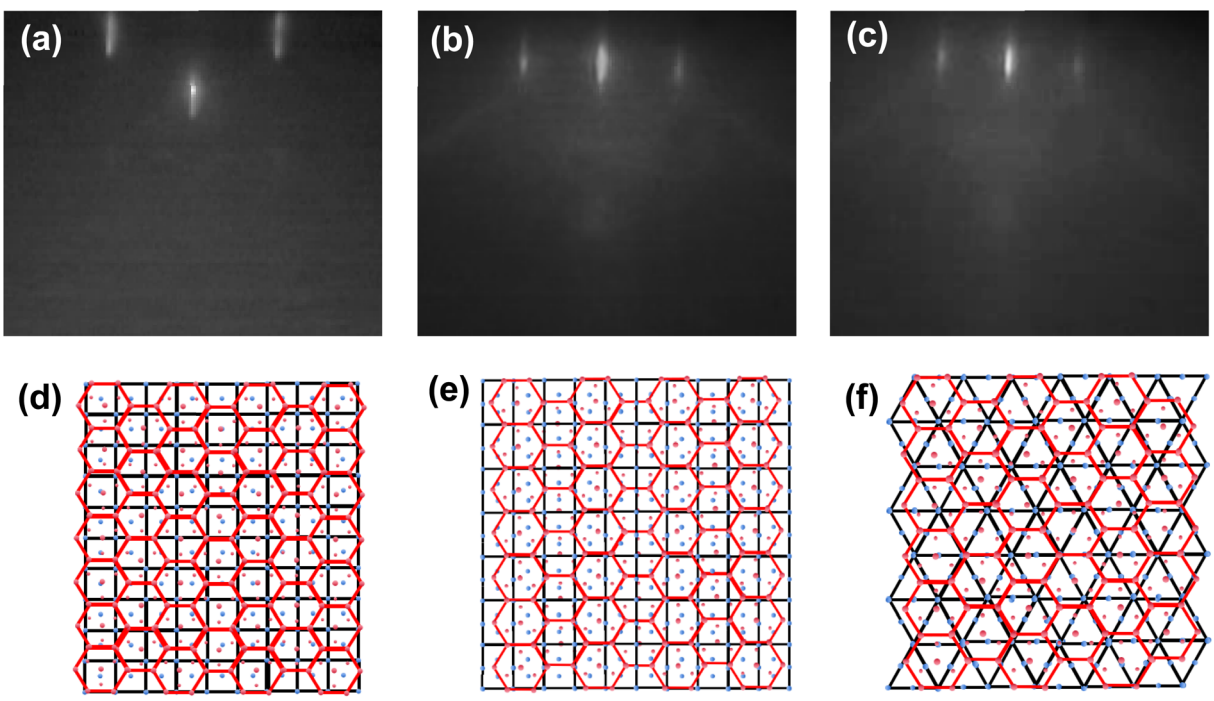

Fig. 4 RHEED diffraction pattern of the Si substrates: (a) Si(100); (b) Si(110); (c) Si(111). Matching model of Bi and Si substrates: (d) Si(100); (e) Si(110); (f) Si(111).

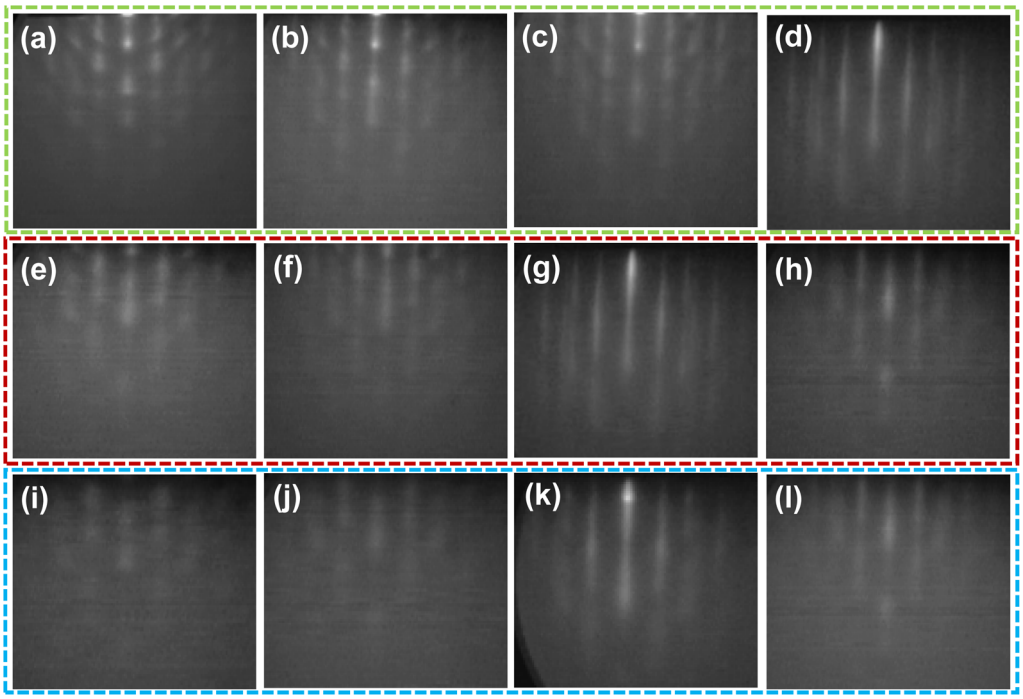

Fig. 5 RHEED patterns of Bi films on Si(100) at: (a) 90 Å, (b) 120 Å, (c) 150 Å, (d) 180 Å; on Si(110) at: (e) 90 Å, (f) 120 Å, (g) 150 Å, (h) 180 Å; and on Si(111) at: (i) 90 Å, (j) 120 Å, (k) 150 Å, (l) 180 Å.

Å, 4.528 Å, 4.535 Å, and 4.546 Å, respectively. On Si(110) substrates, the lattice constants for different Bi film thicknesses are 4.508 Å, 4.533 Å, 4.537 Å, and 4.546 Å. On Si(111) substrates, the lattice constants are 4.513 Å, 4.529 Å, 4.535 Å, and 4.546 Å. When the film thickness is less than 150 Å, the lattice constants are significantly smaller than the bulk bismuth lattice constant of 4.546 Å. This indicates that Bi films on all three Si substrates experience in-plane compressive stress, with greater stress occurring at thinner film thicknesses. As the thickness increases, the RHEED patterns begin to exhibit systematic changes. The spacing between diffraction fringes gradually decreases. According to RHEED diffraction geometry, the fringe spacing is inversely proportional to the interplanar spacing. Therefore, the decrease in fringe spacing directly corresponds to an increase in the in-plane lattice constant. This change indicates that beyond 150 Å, the in-plane stress in the film is released, allowing it to recover toward the equilibrium lattice constant of its bulk material. It is worth noting that strain relaxation and recovery of bulk-like transport are not synonymous. While the lattice constant recovers beyond the critical thickness, the relaxation process inevitably introduces a "defect legacy"—specifically, grain boundaries and dislocations—that persists even in thicker films. These defects act as strong scattering centers and reduce the carrier mean free path, which can significantly modify the transport behavior.

Fig. 6 shows the lattice constants of Bi films with varying thicknesses on the three different substrates, calculated using RHEED. It can be observed that during the first stage, between 90 Å and 150 Å film thicknesses, the Bi lattice constant gradually increases. The second stage occurs when the thickness exceeds

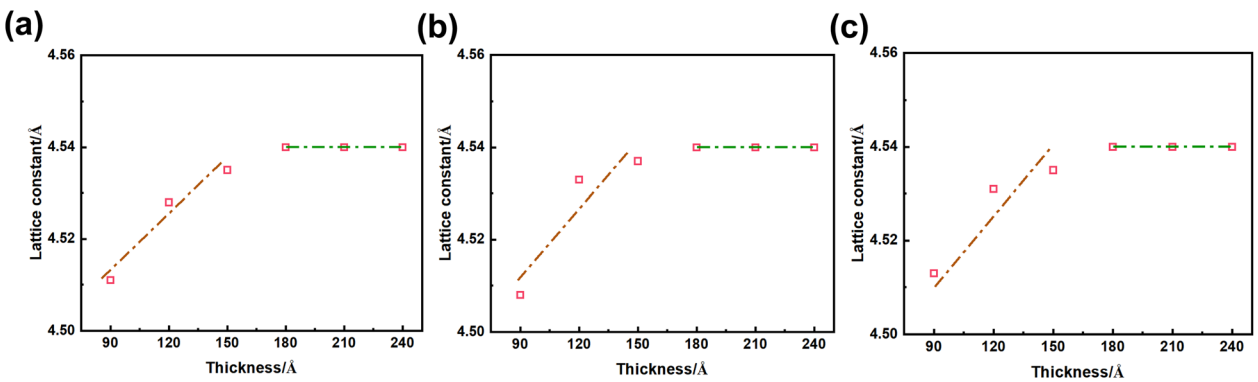

Fig. 6 Lattice constants of Bi films as a function of film thickness: (a) Si(100); (b) Si(110); (c) Si(111).

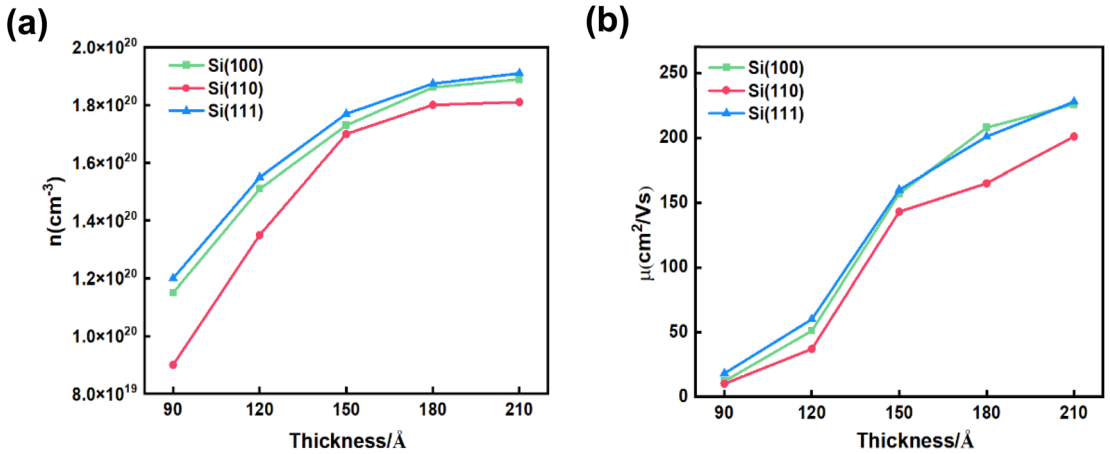

Fig. 7 (a) Carrier density n and (b) mobility μ of Bi films with different thicknesses on the three substrates at 300 K.

150 Å, at which point the Bi lattice constant stabilizes and no longer changes relative to bulk Bi. Based on the half-width and grain size determined by XRD characterization, 150 Å is identified as the critical thickness for Bi/Si films. From the lattice constant variation curve, it can be inferred that, in the first stage, in-plane stress is the primary factor influencing the crystallinity of the Bi film. The crystallinity of the Bi film increases rapidly with a steep curve slope, while the contribution from the grain size is relatively minor. In the second stage, the in-plane stress in the film is released, causing its contribution to decrease rapidly, while the contribution from the grain size gradually increases. However, the influence of the grain size is not significant, resulting in a very small curve slope.

To verify the microscopic mechanism of carrier behavior, Hall effect measurements were performed on Bi films grown on three substrates using the van der Pauw method, as shown in Fig. 7. Both carrier concentration and mobility exhibited thickness dependence, a variation closely related to the stress release process. The three-dimensional electron (hole) density is defined as $n(P)$. Fig. 7a and b display the mobility and carrier density of various carriers in a perpendicular magnetic field for the three substrates. As the thickness increases, the carrier concentration and mobility of bismuth films on the three substrates exhibit a rapid growth trend before reaching the critical thickness, followed by a saturation trend beyond the critical thickness. Below 150 Å, compressive stress increases the separation energy between light and heavy hole bands and may slightly broaden the bandgap, significantly suppressing intrinsic carrier excitation. Beyond this thickness, the lattice constant gradually recovers, enhancing the overlap of

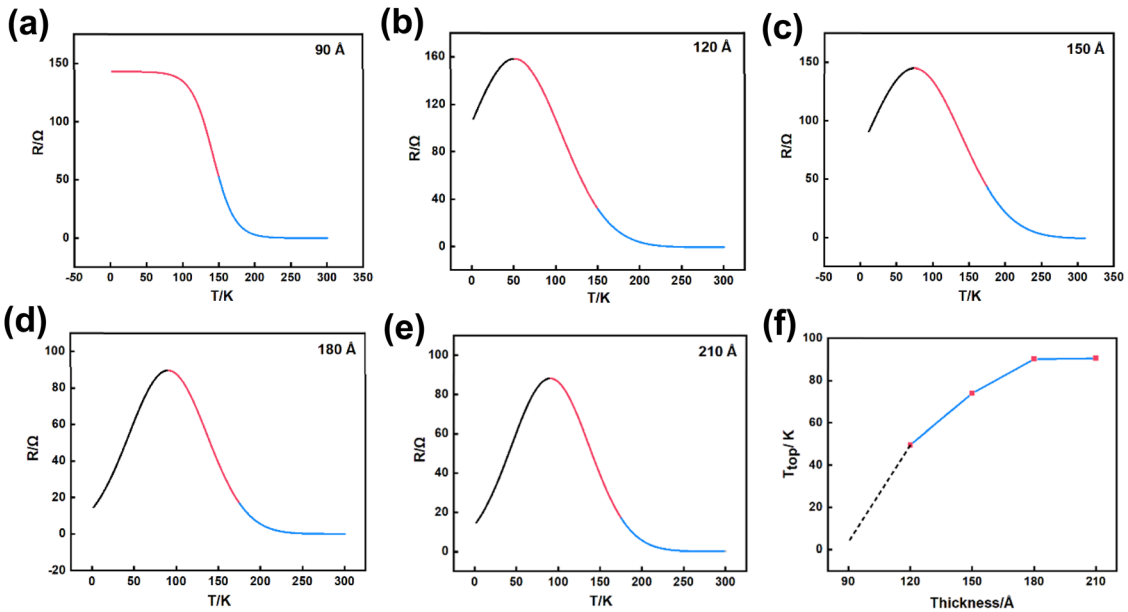

Fig. 8 Temperature dependent resistance curves of Bi films with different thicknesses on Si(100). (a) 90 Å, (b) 120 Å, (c) 150 Å, (d) 180 Å, and (e) 210 Å and (f) T_{top} curve as a function of thickness for Bi films.

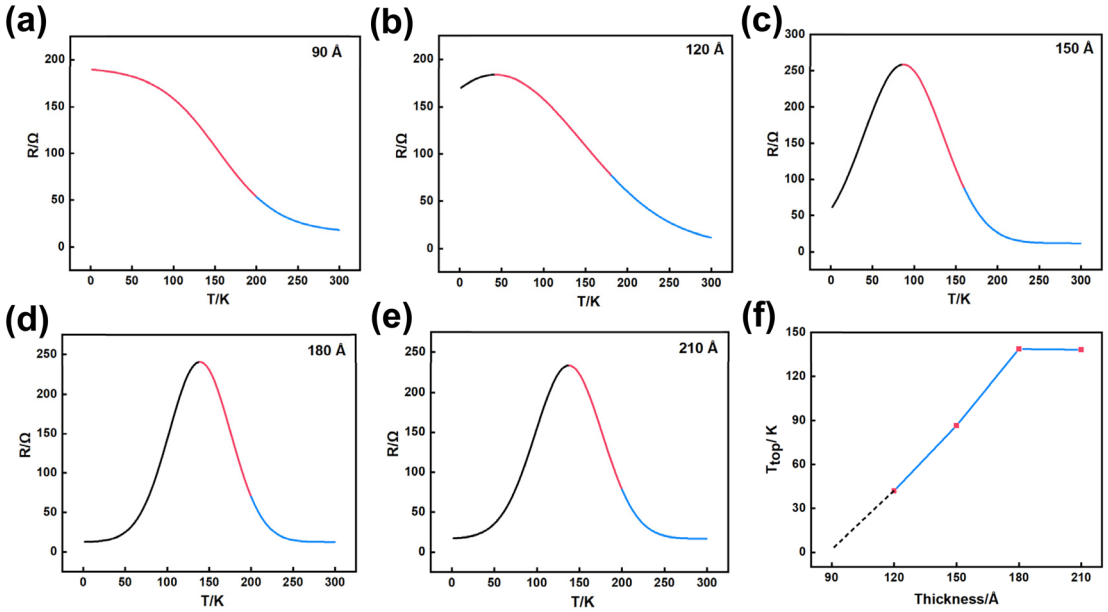

Fig. 9 Temperature dependent resistance curves of Bi films with different thicknesses on Si(110): (a) 90 Å, (b) 120 Å, (c) 150 Å, (d) 180 Å, and (e) 210 Å and (f) T_{top} curve as a function of thickness for Bi films.

semimetallic intrinsic bands and exciting more intrinsic electrons and holes. After 150 Å, carrier concentration further increases to levels approaching those of bulk bismuth materials. The elevated carrier density in our films, particularly in the thicker samples, may indeed indicate an extrinsic contribution beyond pure strain effects. One plausible mechanism is charge transfer from the Si substrate or interfacial states. The Si/Bi interface can act as a source of excess carriers, thereby doping the Bi film. The Hall effect clearly maps the evolution of physical properties in Bi films on Si substrates with increasing thickness. Starting from a stress-constrained state characterized by low carrier concentration, low mobility semiconducting behavior, the films undergo a critical thickness transition zone before ultimately transitioning to a stress-released state marked by high carrier concentration and high electron mobility semimetallic behavior.

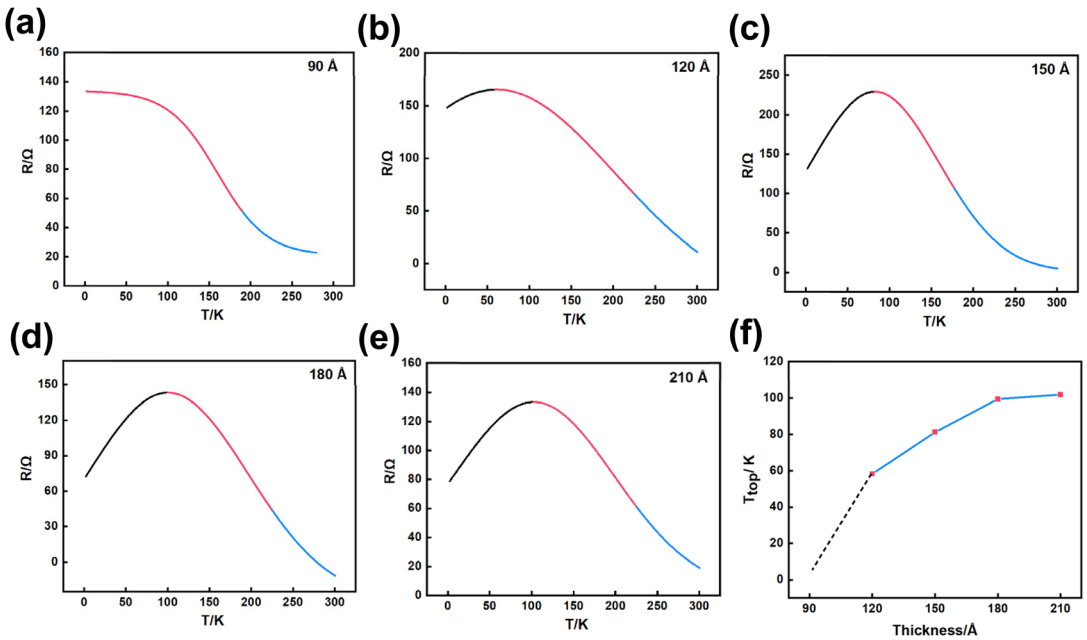

Fig. 10 Temperature dependent resistance curves of Bi films with different thicknesses on Si(111): (a) 90 Å, (b) 120 Å, (c) 150 Å, (d) 180 Å, (e) 210 Å and (f) T_{top} curve as a function of thickness for Bi films.

To further investigate the effect of mismatch stress on the transport properties of Bi films, the transport characteristics of Bi films with varying thicknesses on the three different substrates were measured. Fig. 8 displays the *R–T* curves and variation curves of the resistance peak T_{top} for Bi films of different thicknesses on Si(100) substrates. Within the Bi films, the *R–T* curve exhibits a resistance peak in the low-temperature region. This peak originates from Bi's unique semimetallic band structure and carrier competition. As shown in Fig. 8a–e, the *R–T* curves of Bi epitaxial films exhibit three distinct transport mechanisms: the high-temperature phase (blue curve) displays semiconductor-like resistance, increasing linearly with decreasing temperature. The low-temperature phase (black curve) exhibits metallic resistance, decreasing linearly with decreasing temperature. The intermediate competition phase (red curve) shows mixed resistance behavior. It can be observed that as the thickness increases, the metallic state characteristics of the Bi film gradually emerge while the semiconductor state characteristics diminish. The resistivity peak in our thick films is interpreted as a combined effect of (i) the intrinsic semimetallic band structure (competition between light holes and electrons), and (ii) extrinsic grain boundary scattering that modifies the temperature dependence. When the Bi film is subjected to compressive stress, the metallic state of Bi is suppressed or even eliminated, causing it to exhibit semiconductor state characteristics. Upon stress release, the Bi film gradually regains the metallic state characteristics of bulk-like bismuth, with resistance showing a slight increase with rising temperature—a characteristic weak metallic behavior of the bulk Bi material. Below the critical thickness, the Bi film experiences compressive stress, increasing the light/heavy hole band separation energy and significantly suppressing intrinsic carrier excitation, causing the film to exhibit semiconductor behavior. As the thickness increases beyond the critical value, stress is released and the lattice constant gradually recovers toward bulk bismuth values. This macroscopically manifests as the previously suppressed metallic state becoming accessible. As shown in Fig. 8f, as the thickness increases, T_{top} increases from 49.5 K to 90.5 K. This indicates that the film thickness directly influences the transition between the metallic and semiconducting states of the Bi film. The shift of T_{top} toward higher temperatures with increasing film thickness suggests that the transition temperature for the metallic state gradually increases, the metallic characteristics progressively strengthen, and the semiconducting state occupies a smaller proportion in the competition. Fig. 9 and 10 show the *R–T* curves and T_{top} curves for Bi films on Si(110) and Si(111) substrates, respectively. The *R–T* curve exhibits the same trend as that observed for Bi films on Si(100) substrates. The T_{top} of the Bi film on the Si(110) substrate increases from 41.9 K to 138.2 K with increasing thickness. For Bi films on Si(111) substrates, T_{top} increases from 58.9 K to 101.8 K with thickness. At thin film thicknesses, the lattice mismatch between the substrate and film induces significant internal stress. As the thickness increases, stress is gradually released, altering Bi's electronic structure and shifting T_{top} toward higher temperatures. This stress release progressively enhances the metallic state's competitiveness within the Bi film. The three substrates Si(100), Si(110), and Si(111) exhibit different mismatch ratios with Bi films due to their varying lattice orientations. Among them, Si(110) has the highest mismatch and strongest initial strain, resulting in more pronounced semiconductor behavior in the thin-film layer and a more pronounced recovery of metallic properties after stress relaxation. Si(111) exhibits optimal lattice matching due to its hexagonal symmetry, resulting in minimal mismatch and the most stable structural evolution with a narrower range of T_{top} variation; Si(100) lies between these two extremes. These differences directly influence the electronic transport evolution pathways of the Bi film by regulating stress states and their release behavior, confirming the pivotal role of substrate engineering in modulating the physical properties of topological materials.

Conclusion

This study systematically characterized Bi films of varying thicknesses grown on Si(100), Si(110), and Si(111) substrates, successfully revealing the regulation mechanism by which mismatch-induced stress and its relaxation dynamics govern the electronic structure and transport properties of epitaxial Bi films. RHEED and XRD results confirm the compressive stress induced by lattice mismatch and its relaxation above a critical thickness of ~150 Å, further determining the matching patterns between Bi and the substrate. Below the critical thickness, the Bi film experiences compressive stress, increasing the light/heavy hole band separation energy and significantly suppressing intrinsic carrier excitation, causing the film to exhibit semiconductor behavior. As the thickness increases beyond the critical value, stress is released and the lattice constant gradually recovers toward bulk bismuth values. This macroscopically manifests as the previously suppressed metallic state becoming accessible. The Hall effect measurements show that the electron concentration and mobility increase and approach saturation. Ultimately, electrical transport properties transition from semiconducting to metallic states, with *R–T* curves exhibiting characteristic bulk-like bismuth behavior where T_{top} shifts toward higher temperatures. The most significant discovery of this study lies in establishing a clear "stress–electronic structure–transport properties" correlation chain, demonstrating that mismatch stress serves as an effective "tool" for precisely controlling the physical state of topological semimetals. This provides a solid theoretical and experimental foundation for developing next-generation silicon-based thermoelectric and spintronic devices.

Conflicts of interest

There are no conflicts to declare.

Data availability

The data that support the findings of this study are included within the article.

Acknowledgements

This work was supported by the National Natural Science Foundation of China (No. 61971116 and 12574242), the Fundamental Research Funds for the Central Universities (No. N25XQD025), the China Postdoctoral Science Foundation (No. 2025M780029) and the Natural Science Foundation of Liaoning Province (Doctoral Research Start-up Fund Project, No. 2025-BS-0087).

References

1 E. Aktürk, O. Ü. Aktürk and S. Ciraci, Single and bilayer bismuthene: stability at high temperature and mechanical and electronic properties, *Phys. Rev. B*, 2016, **94**, 014115.
2 N. Wang and Y. Qi, Enhanced transport properties of Bi thin film by preferential current flow pathways in low angle grain boundaries, *Vacuum*, 2019, **169**, 108874.
3 N. Wang, T. Zhang, B. W. Zhang and N. Zhang, Optimization of large magnetoresistance of polycrystalline Bi film, *Vacuum*, 2023, **213**, 112095.
4 T. Nagao, T. Doi, T. Sekiguchi and S. Hasegawa, Epitaxial growth of single-crystal ultrathin films of bismuth on Si(111), *Jpn. J. Appl. Phys.*, 2000, **39**, 4567–4570.
5 T. Nagao, J. T. Sadowski, M. Saito, S. Yaginuma, Y. Fujikawa, T. Kogure, T. Ohno, Y. Hasegawa, S. Hasegawa and T. Sakurai, Nanofilm allotrope and phase transformation of ultrathin Bi film on Si(111)-7×7, *Phys. Rev. Lett.*, 2004, **93**, 105501.
6 M. Hase, K. Ishioka, M. Kitajima, K. Ushida and S. Hishita, Dephasing of coherent phonons by lattice defects in bismuth films, *Appl. Phys. Lett.*, 2000, **76**, 1258–1260.
7 N. Wang, Y. X. Dai, T. L. Wang, H. Z. Yang and Y. Qi, Investigation of growth characteristics and semimetal-semiconductor transition of polycrystalline bismuth thin films, *IUCrJ*, 2020, **7**, 49–57.
8 K. Nagase, I. Kokubo, S. Yamazaki, K. Nakatsuji and H. Hirayama, Structure and growth of Bi(110) islands on Si(111)3×3-Bsubstrates, *Phys. Rev. B*, 2018, **97**, 195418.
9 G. Sant'ana, D. Möckli, A. Cas Viegas, P. Pureur and M. A. Tumelero, Ni/Bi bilayers: The effect of thickness on the superconducting properties, *J. Appl. Phys.*, 2024, **135**, 043905.
10 N. Kawakami, C.-L. Lin, M. Kawai, R. Arafune and N. Takagi, One-dimensional edge state of Bi thin film grown on Si(111), *Appl. Phys. Lett.*, 2015, **107**, 031602.
11 P. Hofmann, The surfaces of bismuth: structural and electronic properties, *Prog. Surf. Sci.*, 2006, **81**, 191–245.
12 F. Jona, Low-energy electron diffraction study of surfaces of antimony and bismuth, *Surf. Sci.*, 1967, **8**, 57–76.
13 T. Hirahara, I. Matsuda, S. Yamazaki, N. Miyata, S. Hasegawa and T. Nagao, Large surface-state conductivity in ultrathin Bi films, *Appl. Phys. Lett.*, 2007, **91**, 202106.
14 L. Kumari, J. H. Lin and Y. R. Ma, Laser oxidation and wide-band photoluminescence of thermal evaporated bismuth thin films, *J. Phys. D Appl. Phys.*, 2008, **41**, 024405.
15 D. Tishkevich, S. Grabchikov, T. Zubar, D. Vasin, S. Trukhanov, A. Vorobjova, D. Yakimchuk, A. Kozlovskiy, M. Zdorovets, S. Giniyatova, D. Shimanovich, D. Lyakhov, D. Michels, M. Dong, S. Gudkova and A. Trukhanov, Early-stage growth mechanism and synthesis conditions-dependent morphology of nanocrystalline Bi films electrodeposited from perchlorate electrolyte, *Nanomaterials*, 2020, **10**, 1245.
16 T. Nagao, J. Sadowski, M. Saito, S. Yaginuma, Y. Fujikawa, T. Kogure, T. Ohn, Y. Hasegawa, S. Hasegawa and T. Sakurai, Nanofilm allotrope and phase transformation of ultrathin Bi film on Si(111)-7×7, *Phys. Rev. Lett.*, 2004, **93**, 105501.
17 C. A. Hoffman, J. R. Meyer, F. J. Bartoli, A. D. Venere, X. J. Yi, C. L. Hou, H. C. Wang, J. B. Ketterson and G. K. Wong, Semimetal-to-semiconductor transition in bismuth thin films, *Phys. Rev. B: Condens. Matter Mater. Phys.*, 1993, **48**, 11431–11434.
18 N. Wang, J. Zhang and Y. Qi, Growth condition effects on the structure evolution and electrical properties of low-melting-point bismuth films, *CrystEngComm*, 2022, **24**, 3576–3585.
19 R. Koseva, I. Mönch, D. Meier, J. Schumann, K. Arndt, L. Schultz, B. Zhao and O. Schmidt, Evolution of hillocks in Bi thin films and their removal upon nanoscale mechanical polishing, *Thin Solid Films*, 2012, **520**, 5589–5592.
20 S. Xiao, D. Wei and X. Jin, Bi(111) thin film with insulating interior but metallic surfaces, *Phys. Rev. Lett.*, 2012, **109**, 166805.
21 H. Abe, D. Iwasawa, M. Imamura, K. Takahashi and A. Takayama, Electronic structure of Sb ultrathin film on Bi(111) with large lattice mismatch, *AIP Adv.*, 2023, **13**, 055303.
22 P. A. Gabrys, S. E. Seo, M. X. Wang, E. Oh, R. J. Macfarlane and C. A. Mirkin, Lattice mismatch in crystalline nanoparticle thin films, *Appl. Nano Lett.*, 2018, **18**, 579–585.
23 S. Stanionytė, T. Malinauskas, G. Niaura, M. Skapas, J. Devenson and A. Krotkus, The crystalline structure of thin bismuth layers grown on silicon (111) substrates, *Materials*, 2022, **15**, 4847.
24 D. B. Kim, J. Y. Kim, J. Han and Y. S. Cho, Strain engineering in power-generating and self-powered nanodevices, *Nano Energy*, 2024, **125**, 109551.
25 Z. E. Zhang, C. Xie, J. Zhang, J. M. He, T. F. Ma and Q. H. Fang, Effects of material mismatch on interfacial cracking of ferroelectric film/substrate structures, *Eng. Fract. Mech.*, 2018, **201**, 261–268.
26 X. Y. Hu, L. L. Kerr, X. S. Zhao, C. Ling, Z. J. Zhao, H. B. Jin, Y. J. Zhao and J. B. Li, Thermodynamic modeling of elastic mismatch strain energy on epitaxial growth of GaInN thin films, *J. Alloys Compd.*, 2019, **798**, 112–118.
27 H. Hirayama, Nucleation and growth of ultrathin Bi films, *Adv. Phys.: X*, 2021, **6**, 1845975.
28 G. Pető, G. Molnár, Z. Horváth, C. Daróczi, É. Zsoldos and J. Gyulai, Formation of epitaxial erbium-silicide islands on Si(001), *Surf. Sci.*, 2005, **578**, 142–148.
29 J. Ohta, H. Fujioka, H. Takahashi, M. Sumiya and M. Oshima, RHEED and XPS study of GaN on Si(111)

grown by pulsed laser deposition, *J. Cryst. Growth*, 2001, **233**, 779–784.
30 D. Yue, W. W. Lin and C. L. Chien, Negligible spin-charge conversion in Bi films and Bi/Ag(Cu) bilayers, *APL Mater.*, 2021, **9**, 050904.
31 Y. Fuseya, M. Ogata and H. Fukuyama, Transport properties and diamagnetism of Dirac electrons in bismuth, *J. Phys. Soc. Jpn.*, 2015, **84**, 012001.
32 J. Fan and J. Eom, Direct electrical observation of spin Hall effect in Bi film, *Appl. Phys. Lett.*, 2008, **92**, 142101.
33 M. Rudolph and J. J. Heremans, Spin-orbit interaction and phase coherence in lithographically defined bismuth wires, *Phys. Rev. B: Condens. Matter Mater. Phys.*, 2011, **83**, 205410.
34 M. Rudolph and J. J. Heremans, Electronic and quantum phase coherence properties of bismuth thin films, *Appl. Phys. Lett.*, 2012, **100**, 241601.
35 E. Xenogiannopoulou, D. Tsoutsou, P. Tsipas, S. Fragkos, S. Chaitoglou, N. Kelaidis and A. Dimoulas, Ultrathin epitaxial Bi film growth on 2D $HfTe_2$ template, *Nanotechnology*, 2021, **33**, 015701.
36 T. Hirahara, N. Fukui, T. Shirasawa, *et al.*, Atomic and electronic etructure of ultrathin Bi(111) films grown on Bi_2Te_3(111) substrates: evidence for a strain-induced topological phase transition, *Phys. Rev. Lett.*, 2012, **109**, 227401.
37 I. Aguilera, C. Friedrich and S. Blügel, Electronic phase transitions of bismuth under strain from relativistic self-consistent GW calculations, *Phys. Rev. B: Condens. Matter Mater. Phys.*, 2015, **91**, 125129.
38 S. Hosoi, F. Tachibana, M. Sakaguchi, K. Ishida, M. Shimozawa, K. Izawa, Y. Fuseya, Y. Kinoshita and M. Tokunaga, Effects of strain-tunable valleys on charge transport in bismuth, *Phys. Rev. Res.*, 2024, **6**, 033096.
39 C. R. Ast and H. Höchst, Electronic structure of a bismuth bilayer, *Phys. Rev. B: Condens. Matter Mater. Phys.*, 2003, **67**, 113102.
40 D. C. Wang, L. Chen, H. M. Liu and X. L. Wang, Electronic structures and topological properties of Bi(111) ultrathin films, *J. Phys. Soc. Jpn.*, 2013, **82**, 094712.
41 C. H. Dong, Y. L. Liu and Y. Qi, Effect of thickness on the surface and electronic properties of Bi Film, *Acta Metall. Sin.*, 2018, **54**, 935–942.
42 S. H. Xiao, D. H. Wei and X. F. Jin, Bi(111) Thin Film with Insulating Interior but Metallic Surfaces, *Appl. Phys. Lett.*, 2012, **109**, 166805.
43 D. Meyer, G. Jnawali, H. Hattab and M. Hoegen, Rapid onset of strain relief by massive generation of misfit dislocations in Bi(111)/Si(001) heteroepitaxy, *Appl. Phys. Lett.*, 2019, **114**, 081601.
44 P. A. Gabrys, S. E. Seo, M. X. Wang, E. B. Oh, R. J. Macfarlane and C. A. Mirkin, Lattice Mismatch in Crystalline Nanoparticle Thin Films, *Nano Lett.*, 2018, **18**, 579–585.
45 M. D. Li and P. Yang, Regulating mismatch strain to improve domain walls conductivity of lithium niobate films, *J. Phys. Chem. Solids*, 2026, **208**, 113075.